Materials Horizons

COMMUNICATION

Heliconical-layered nanocylinders (HLNCs) – hierarchical self-assembly in a unique B4 phase liquid crystal morphology

Received 00th January 20xx,
Accepted 00th January 20xx

DOI: 10.1039/x0xx00000x

www.rsc.org/

Sasan Shadpour,[a] Ahlam Nemati,[a] Nicola Jane Boyd,[b] Lin Li,[c] Marianne Estelle Prévôt,[a] Samantha L. Wakerlin,[a] Julie P. Vanegas,[a] Mirosław Salamończyk,[d,e] Elda Hegmann,[a,g] Chenhui Zhu,[d] Mark R. Wilson,[b] Antal I. Jákli,[a,f] Torsten Hegmann*[a,c]

A unique morphology for bent-core liquid crystals forming the B4 phase has been found for a class of tris-biphenyl bent-core liquid crystal molecules with a single chiral side chain in the longer *para*-side of the molecule. Unlike the parent molecules with two chiral side chains or a chiral side chain in the shorter *meta*-side, which form helical nano- or microfilament B4 phases, the two derivatives described here form heliconical-layered nanocylinders composed of up to 10 coaxial heliconical layers, which can split or merge, braid, and self-assemble into a variety of modes including feather- or herringbone-type structures, concentric rings, or hollow nest-like superstructures. These multi-level hierarchical self-assembled structures, rivaling muscle fibers, display blue structural color and show immense structural and morphological complexity.

Liquid crystals (LCs) with a bent core have revolutionized research in soft condensed matter chemistry and physics. Remarkable research highlights include the discovery of the first smectic fluid composed of achiral molecules exhibiting large homochiral domains that form a chiral conglomerate,[1] dark conglomerate phases with plumber's nightmare three-dimensional super-structure,[2] new nematic liquid crystal phases such as the twist-bend phase,[3] chiral self-sorting and amplification in isotropic liquids of achiral bent-core molecules,[4] and the discovery of the twisted helical nanofilament (HNF) phase[5] with not just one but two chiral twists[6].

Conceptual insights

The morphology is of critical importance for molecular crystals, drug molecules, alloys, and elements in the periodic table. We here demonstrate how very subtle structural changes in a set of bent-core liquid crystals lead to rather complex hierarchical superstructures driven by changes in molecular conformation. By relocating one or two methyl groups, thereby strategically introducing chiral centers, the growth of helical nanofilaments, helical microfilaments, or heliconical-layered nanocylinders is observed, all with a B4 phase structure. All phases are chiral, either in the form of a chiral conglomerate or homochiral, and exhibit blue structural color. Imaging of the heliconical-layered nanocylinder morphology using electron and atomic force microscopy reveals six levels of hierarchical self-assembly, from layer packing to intricate 3D shapes, rivaling complex filaments found commonly only in biological systems.

The HNF or classical B4 phase is a remarkable display of self-assembly guided by molecular conformation. The classic description of the B4 phase was that of a crystalline phase.[7] More recent work demonstrates that the B4 phase is neither a traditional crystalline solid nor a conventional liquid crystal phase.[8] The phase forms due to an intra-layer mismatch between the two molecular halves that can only be relieved by local saddle-splay, ultimately leading to twisted filaments composed of a limited number of layer stacks (about 5 - 7 layers). The resulting porous filaments then assemble into a loose hexatic liquid crystalline structure.[8, 9] In the case of achiral molecules, HNF phases form a conglomerate composed of macroscopic chiral domains. Subtle modifications of the molecular structure led to the discovery of a modulated HNF phase (HNF_{mod}) featuring an additional intralayer electron-density modulation.[8] B4 phases based on the HNF morphology have tremendous potential for applications including photovoltaics, chiral amplification, and chiral separation due to their unique ability to serve as porous nanotemplates with chiral surfaces.[10] A dual modulated HNF phase (HNF_{mod2}) with additional intra- and interlayer modulations, introduced by adding chiral centers to both aliphatic chains of tris-biphenyl

[a] Chemical Physics Interdisciplinary Program, Advanced Materials and Liquid Crystal Institute, Kent State University, Kent (Ohio) 44242-0001 USA.
[b] Department of Chemistry, Durham University, Durham, DH1 3LE, UK
[c] Department of Chemistry and Biochemistry, Kent State University, Kent (Ohio) 44242-0001 USA.
[d] Advanced Light Source, Lawrence Berkeley National Laboratory, Berkeley (CA) 94720 USA.
[e] Faculty of Chemistry, University of Warsaw, 02-089 Warszawa, Poland.
[f] Department of Physics and Astronomy, Kent State University, Kent (Ohio) 44242-0001 USA.
[g] Department of Biological Sciences, Kent State University, Kent (Ohio) 44242-0001 USA

Electronic Supplementary Information (ESI) available: Synthesis details and full characterization of all compounds, experimental setups, procedures and techniques as well as additional POM, DSC, AFM, SEM, TEM, UV-vis, XRD, and molecular dynamics simulation data. See DOI: 10.1039/x0xx00000x

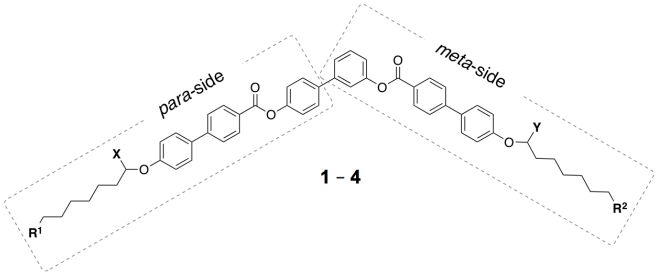

Name	X / R¹	Y / R²	Cooling / heating rate	Phase sequence (morphology) and phase transition temperatures / °C
1	H / CH_3	H / CH_3	slow	Iso $\underset{187.6}{\overset{183.4}{\rightleftharpoons}}$ Col_r $\underset{170.5}{\overset{158.9}{\rightleftharpoons}}$ B4 (HNF_{mod})
(*R*,*R*)-**2**	(*R*)-CH_3 / H	(*R*)-CH_3 / H	slow	Iso $\underset{120.2}{\overset{104.5}{\rightleftharpoons}}$ B4 (HNF_{mod2}) $\overset{94.2}{\leftarrow}$ Cr
(*S*,*S*)-**2**	(*S*)-CH_3 / H	(*S*)-CH_3 / H	slow	Iso $\underset{120.7}{\overset{106.1}{\rightleftharpoons}}$ B4 (HNF_{mod2}) $\overset{94.2}{\leftarrow}$ Cr
m-(*R*)-**3**	H / CH_3	(*R*)-CH_3 / H	slow	Iso $\underset{152.8}{\overset{139.9}{\rightleftharpoons}}$ Col_{ob}
			rapid	Iso $\underset{152.3}{\overset{128.4}{\rightleftharpoons}}$ B4 (HμF)
m-(*S*)-**3**	H / CH_3	(*S*)-CH_3 / H	slow	Iso $\underset{152.8}{\overset{139.9}{\rightleftharpoons}}$ Col_{ob}
			rapid	Iso $\underset{152.3}{\overset{128.4}{\rightleftharpoons}}$ B4 (HμF)
p-(*R*)-**4**	(*R*)-CH_3 / H	H / CH_3	slow	Iso $\underset{156.6}{\overset{146.7}{\rightleftharpoons}}$ Col_r $\underset{Col_{ob}\ 151.2}{\overset{138.1}{\rightarrow}}$ B4 (HLNC)
			rapid	Iso $\underset{153.3}{\overset{142.6}{\rightleftharpoons}}$ Col_r $\overset{132.7}{\rightarrow}$ Col_r + B4 (HLNC)
p-(*S*)-**4**	(*S*)-CH_3 / H	H / CH_3	slow	Iso $\underset{156.6}{\overset{146.7}{\rightleftharpoons}}$ Col_r $\underset{Col_{ob}\ 151.2}{\overset{138.1}{\rightarrow}}$ B4 (HLNC)
			rapid	Iso $\underset{153.3}{\overset{142.6}{\rightleftharpoons}}$ Col_r $\overset{132.7}{\rightarrow}$ Col_r + B4 (HLNC)

Scheme 1. Chemical structure, phase sequence, and morphology (of the B4 phase) depending on heating/cooling rate, and phase transition temperatures of the bent-core LCs **1** – **4** (from 2nd heating/cooling run by DSC; at 5 °C min^{-1} for slow and 50 °C min^{-1} for rapid heating/cooling). Compound **1**[8] lacking a chiral center and compounds **2**[11] with two chiral centers of identical absolute configuration are the parent LCs, respectively. Compounds **3**[12] and **4** have only one chiral center either on the *meta*- or the *para*-side of the molecule.

(tris-BiPh) B4 phase forming bent core LCs with identical absolute configuration (homochiral), resulted in homochiral HNF_{mod2} phases with matching secondary twist.[11] A thus far unobserved type of polymorphism (i.e. the ability of a solid material to exist in more than one form of crystal structure) was reported for such tris-BiPh bent-core LCs when the chiral center was exclusively introduced at the *meta*-side of these molecules. In this case, the formation of entirely different phase structures solely depending on the rate of cooling from the isotropic liquid phase was found. Upon rapid cooling a unique morphology of helical microfilaments (HμFs) was formed, while slow cooling resulted in an oblique columnar (Col_{ob}) phase.[12]

Here we report on a hierarchically self-assembled, rather unique B4 phase morphology that has heretofore not been reported. These heliconical-layered nanocylinders (HLNCs) form for the almost identical tris-BiPh bent-core molecules when the chiral center was introduced at the *para*-side (Scheme 1). Rather than twisted, the layers are now rolled up in a heliconical fashion to form optically active nanocylinders. Layers with a thickness of ~ 4 nm, i.e. about one molecular length, are rolled up into ~ 80 nm diameter coaxial cylinders made up of ~ 10 layers. The phase appears when the sample is cooled slowly from the isotropic liquid phase (5 °C min^{-1}), while a biphasic regime composed of a columnar (Col) and the B4 phase is formed upon quenching the sample thermally from the isotropic liquid phase, adding a complex morphology to those already observed for these tris-BiPh derivatives. Provided ample time for nucleation, growth, and self-assembly, these HLNCs form a remarkable highly ordered

phase superstructure with additional self-assembly modes depending on sample conditions such as the sample thickness.

A set of experimental techniques including polarized light optical microscopy (POM), differential scanning calorimetry (DSC), scanning electron and transmission electron microcopy (SEM, TEM), circular dichroism (CD) spectropolarimetry, atomic force microscopy (AFM), and X-ray diffraction (incl. synchrotron small angle X-ray diffraction, SAXD) were used to study the thermal and optical properties as well as the structure. Moreover, a set of computational methods including density functional theory (DFT) methods, stochastic dynamics (SD) atomistic simulations, and molecular dynamics (MD) bulk phase simulations were employed to better understand the underlying molecular origins leading to the various formed 3D morphologies.

Scheme 1 gives the generalized chemical structure of the tris-BiPh bent-core derivatives as well as the phase sequences and phase transition temperatures depending on the pattern of non-branched achiral and branched chiral side chains. The synthesis of the precursor compounds provided in Scheme S1 (ESI) was described earlier.[11, 12] Likewise, the synthesis of *p*-(*R*)-**4** and *p*-(*S*)-**4** involves a stepwise deprotection/esterification of mono-tetrahydropyranyl (THP)—mono-*tert*-butyldimethylsilyl (TBDMS)-protected 3,4'-dihydroxybiphenyl prepared prior via a Suzuki cross-coupling reaction[13, 14] (ESI, Sections 1 – 4).

POM provides the initial evidence for the heretofore not reported B4 phase HLNC morphology. Fig. 1 shows the thin-film textures recorded upon cooling and heating for *p*-(*R*)-**4** and *p*-(*S*)-**4** sandwiched between two pre-cleaned glass substrates. Fig. 1a shows the low birefringence fan-like texture observed for *p*-(*R*)-**4** upon slow cooling (at 5 °C min^{-1}) from the isotropic liquid phase to room temperature. Decrossing the polarizers by several degrees in either direction does not produce any change in color for any of the domains, and images taken with a quarter wave plate (Fig. S13, ESI) suggest a tangential orientation of the building blocks in these domains (revealed by other imaging techniques later). Upon reheating the sample, the texture changes to a distinct, colorful fan-like or spherulitic texture, frequently reported for Col_{ob} phases of bent-core LCs,[15] which then clears to the isotropic liquid phase upon further heating (Fig. 1b). Remarkably, a different, now mosaic texture typical for Col_r phases appears in the next cooling cycle (Fig. 1c).[15] Heating again to the isotropic liquid phase and thermally quenching the sample ultimately produces a biphasic texture with characteristic features of both the initial low-temperature phase as well as the high-temperature Col_r phase (Fig. 1d) found on slow cooling, i.e. radial fan-like and the high birefringence mosaic domains. The other enantiomer *p*-(*S*)-**4** displays a strikingly similar texture sequence depending on the sample's heating/cooling conditions (Figs. 1e-h). Additional POM images for *p*-(*R*)-**4** and *p*-(*S*)-**4** are provided in the ESI (Section 5, Figs. S13 – S15).

DSC measurements performed for both compounds, *p*-(*R*)-**4** and *p*-(*S*)-**4**, using two different heating/cooling rates (slow heating/cooling at 5 °C min^{-1} and fast heating/cooling at 50 °C min^{-1}) are shown in the ESI (Section 6, Table S1 and Fig. S16). The data support the POM results, showing quasi-identical phase behavior for the two enantiomers on slow and rapid heating/cooling, respectively. Noteworthy is the absence of a phase transition peak from the low temperature to the high-temperature Col phase in the rapid heating run already noticed by POM. As expected, the phase transitions are also broader. Since a narrow temperature range characterizes the Col phase on slow heating (about 5 °C), the rapid heating rate appears to suppress the exclusive formation of this phase. Instead a coexistence of the low- and high-temperature phase that was already seen by POM upon rapid cooling to room

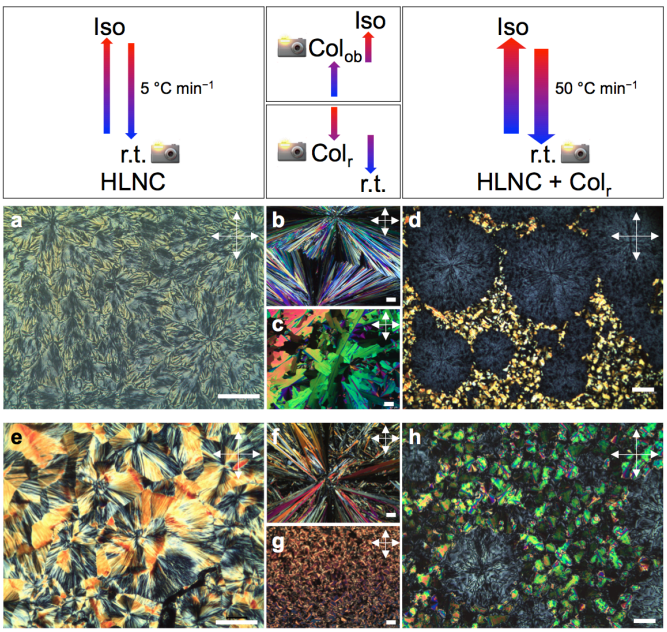

Fig. 1. Polarized optical photomicrographs (crossed polarizers) depending on the sample heating/cooling protocol (depicted schematically above) of (a-d) *p*-(*R*)-**4** and (e-h) *p*-(*S*)-**4**. Images (a), (d), (e), and (h) were taken at room temperature (r.t.), (b) on heating at 145 °C, (c) on cooling at 150 °C, (f) on heating at 144 °C, (g) on heating at 151 °C. Scale bars are 100 µm each.

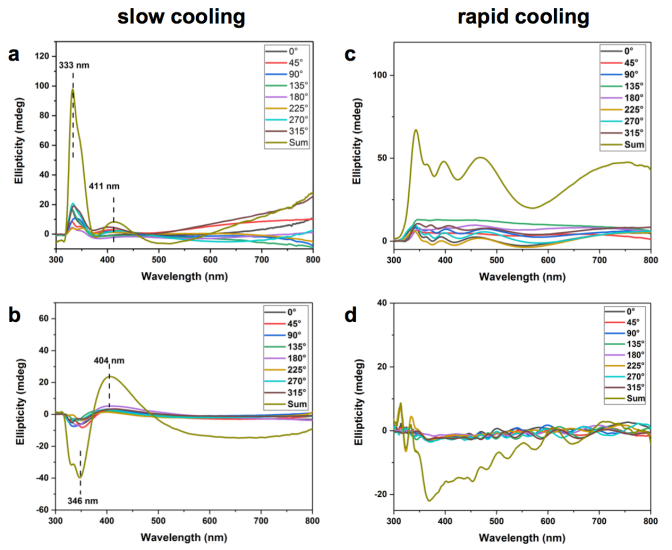

Fig. 2. Thin film CD spectra (film thickness: 10 µm) of: (a, c) *p*-(*R*)-**4** and (b, d) *p*-(*S*)-**4** on: (a, b) slow and (c, d) rapid cooling from the isotropic liquid phase to room temperature (r.t.). Sum and individual sample rotation spectra are shown.

temperature from the isotropic liquid phase is observed (Figs. 1d and 1h).

Both samples, *p*-(*R*)-**4** and *p*-(*S*)-**4**, were also analyzed by CD spectropolarimetry both in solution as well as in thin films of the bulk material. Thin film CD of the bulk materials has been successfully used to determine the formation of homochirality in B4 HNF textures.[11, 12, 16] Figure 2 shows the thin film CD spectra collected of thin films between quartz substrates. To eliminate (or cancel out) contributions from linear dichroism and birefringence, interrogated sample areas were investigated at all sample rotation angles in 45° intervals. The obtained thin films CD spectra were then summed up to provide genuine CD signals of the sample area. The circular area interrogated by the light beam is approximately 0.4 cm in diameter (given by the instrumental slit size and shape), which is larger than the typical size of domains in HNF phases of achiral molecules and larger than the features observed by POM for these samples (~ 500 µm). Therefore the bulk of the sample is measured and not just a single domain. After slow cooling to r.t. (Figs. 2a and 2b), both materials show intense, characteristically structured thin film CD signals with a band and shoulder at 333 and 346 nm, exclusively positive for *p*-(*R*)-**4** and negative for *p*-(*S*)-**4**, somewhat mirroring each other. For the (*R*)-enantiomer the peak at 333 nm and for the (*S*)-enantiomer the peak at 346 nm is more intense. Both CD spectra show an additional broad, positive signal around 410 nm. These spectra are distinctly different from the CD spectra obtained for HNF and $HNF_{mod(2)}$ phases, which show a single intense, mirror-image CD signal around 360 nm, the sign of this signal depending on the molecular chirality and as a result the sense of the nanofilament twist.[11] Likewise, these spectra are not resembling CD spectra reported for the B4 phase with HµF morphology giving a single intense signal at 412 nm.[12] It seems the first signal captures the chirality of the building blocks considering the mirror symmetry in these thin film CD signals as a result of the opposite absolute configuration of the constituent molecules in their heliconical nanocylinders. The second signal at ~ 410 nm, however, must be related to the packing of the HLNC building blocks in some specific fashion that does not necessarily distinguish the molecular chirality. Imaging of these packing modes by SEM, AFM and TEM will later shine more light on this. On rapid cooling the CD spectra become even more complex, but nevertheless display some mirror relationship for the two enantiomers (Figs. 2c and 2d). The biphasic regime (texture) observed by POM (Figs. 1d and 1h), with domain sizes as large as the area probed by CD, makes the interpretation of these spectra very challenging. To further support our arguments that the thin film CD spectra interrogate the complex morphology and packing of the HLNCs in the bulk B4 phase, we also recorded solution CD spectra for *p*-(*R*)-**4** and *p*-(*S*)-**4** (ESI, Section 7, Fig. S17). These CD spectra show the typical mirror image relationship between a set of enantiomers with quasi all CD bands related to molecular absorptions in the UV spectral region (at wavelengths well below the bands seen in the thin film bulk CD spectra). The shoulder and tail of the CD bands starting at around 320 nm is not associated with the superstructures *p*-(*R*)-**4** and *p*-(*S*)-**4** form in solution (in the form of gels in *n*-hexane upon standing) as reported previously by Hsu and co-workers for related bent core molecules.[17, 18] As we will discuss later, SEM reveals that these superstructures closely resemble the HLNCs formed in the bulk B4 phase (same diameter, heliconical solid and not hollow structures), but are shorter in length.

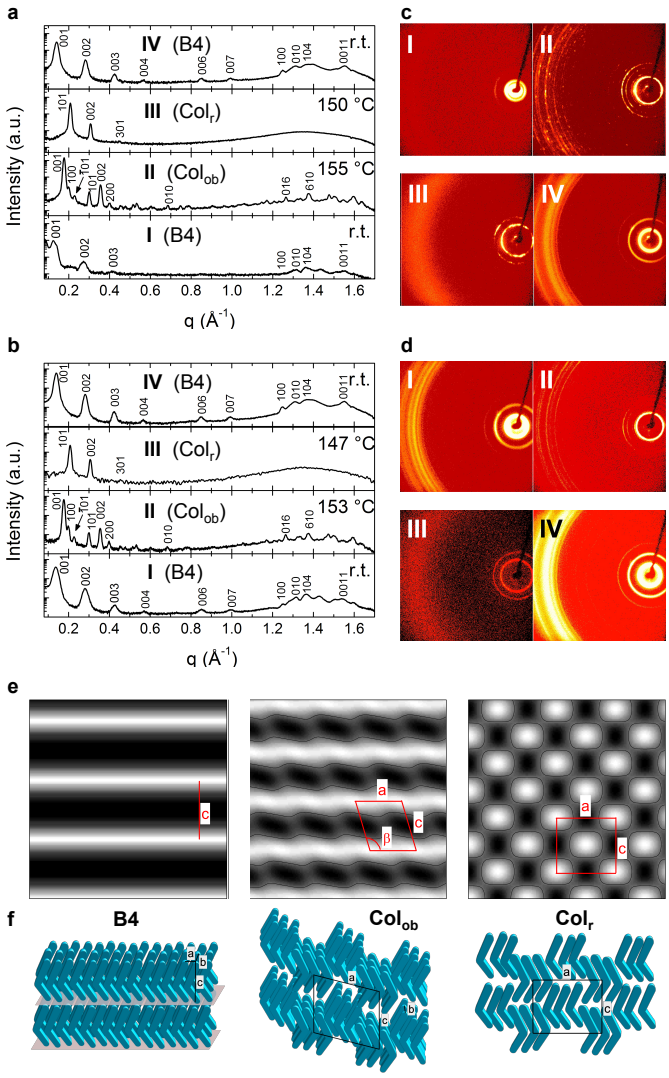

Fig. 3. X-ray diffraction analysis of slow heated and cooled (at 5 °C min^{-1}) samples of: (a, c) *p*-(*R*)-**4** and (b, d) *p*-(*S*)-**4**; (a, b) azimuthally integrated intensity (a.u.) *vs*. *q* (Å^{-1}) of (c, d) the corresponding 2D diffraction patterns. Additional synchrotron small angle X-ray diffraction experiments were used to index the B4 (HLNC) and Col$_{ob}$ phases (see ESI, Section 8, Fig. S18 and Table S2. (e) 2-Dimensional electron density maps reconstructed from X-ray data by reverse Fourier transform of the B4 (HLNC), Col$_{ob}$ and Col$_r$ phases. Maps show *ac* plane. The change from black to white indicates increasing electron density. The modulation in-layer along the 'a' direction for the B4 phase is equal a single molecule and therefore not visible. The size of these maps is 15 × 15 nm^2. The isodensity line is marked to visualize the cross section of the columns. (f) Corresponding molecular models for the B4, Col$_{ob}$ and Col$_r$ phase formed by *p*-(*R*)-**4** and *p*-(*S*)-**4**.

Considering the complex phase behavior determined by POM, structures of all LC phases were characterized in detail by X-ray diffraction (XRD) experiments (see ESI, Section 2 for details). A summary of the XRD results obtained at various temperatures for the observed LC phases on slow and rapid heating/cooling

is provided in Figs. 3a – 3d. As expected for enantiomers, the results for both compounds, *p*-(*R*)-**4** and *p*-(*S*)-**4** are identical. The phase observed at room temperature on a sample not thermally treated (plots **I** in each Fig. 3a and 3b) shows a diffraction pattern typically observed for B4 phases with non-commensurate high *q* peaks that appear to indicate a crystallographic structure within the layers.[19] The structure is orthorhombic with lattice parameters of a = 5.0 Å, b = 4.7 Å, and c = 44.7 Å (c is the layer thickness). One notices that the ratio a/b of ~ 1.06 indicates that the molecular mass centers are distributed nearly in squares within smectic layers. The number of molecules in the unit cell Z is 1. Additionally, the angle between the long (c) and short (a) direction is 90°, which allows us to assume that the long axis of the crystallographic cell is matching the molecular length.

On further heating, a spotted pattern is obtained, which may suggest crystalline character of the phase. However, the POM experiments confirmed its liquid crystalline nature. The observed peaks (plots **II** in each Fig. 3a and 3b) are best indexed with a monoclinic columnar phase (Col_{ob} – $P2$, 3-dimensional) with lattice parameters of a = 32.5 Å, b = 9.1 Å, c = 36.7 Å, and β = 105°. Taking into account the molecular length found in the B4 phase, molecules are now tilted in the Col_{ob} phase by ~ 55°. In this phase Z = 10. Upon further heating to the isotropic liquid phase and cooling back down, the diffraction signals (plots **III** in Figs. 3a and 3b) change and are now best indexed with a rectangular columnar phase (Col_r, $c2mm$, 2-dimensional) with lattice parameters of a = 44.7 Å and c = 40.9 Å with liquid-like short range order indicated by a diffuse high-q peak. The diffraction pattern of the low temperature phase, observed on further cooling to r.t., is virtually identical to the one obtained for the neat samples (plots **IV** in Figs. 3a and 3b). Now, however, up to 7 harmonics are detected. The correlation length calculated from the first peak is equal to 7-8 layers.

Fig. 3e shows the 2-dimensional (ac plane) electron density maps of the B4, Col_{ob}, and Col_r phases reconstructed from the X-ray patterns by reverse Fourier transformation (a 2D body-centered crystallographic unit cell was chosen to calculate the electron density maps),[20] and Fig. 3f shows the corresponding models. In the B4 phase, the molecules are packed in layers with the layer thickness c comparable to the molecular length while both columnar phases show 'broken' layers consisting of blocks. In columnar phases such blocks consist of 5-6 molecules, however, in the Col_r phase adjacent blocks are translated by $c/2$.

Especially the Col_{ob} – Col_r polymorphism, already noticed during the POM investigations, appears highly unusual, adding to the substantial structural complexity observed for this particular set of bent core molecules.

With the POM, CD and XRD data at hand, the next step was to examine the morphology of the building blocks in the B4 phase. XRD data confirm that the formed B4 phase features crystalline layers.[21] Both scanning and transmission electron microscopy (SEM, TEM) as well as atomic force microscopy (AFM) confirm layered structures. Fig. 4 shows representative sets of images, obtained from slow cooling of bulk samples of *p*-(*R*)-**4** and *p*-(*S*)-**4** from the isotropic liquid phase (additional EM images can be found in the ESI, Section 9, Figs. S19 and S20). These SEM images reveal that the building blocks are nanoscale cylinders, several tens of microns long and ~ 80 nm in diameter. These nanocylinders are formed by rolled-up layers, twisted in a heliconical fashion as revealed by high-resolution SEM (Fig. 4a insert). Tapping mode AFM images (obtained by slow cooling from the isotropic liquid phase) support this hypothesis by showing 'peeled' regions of these

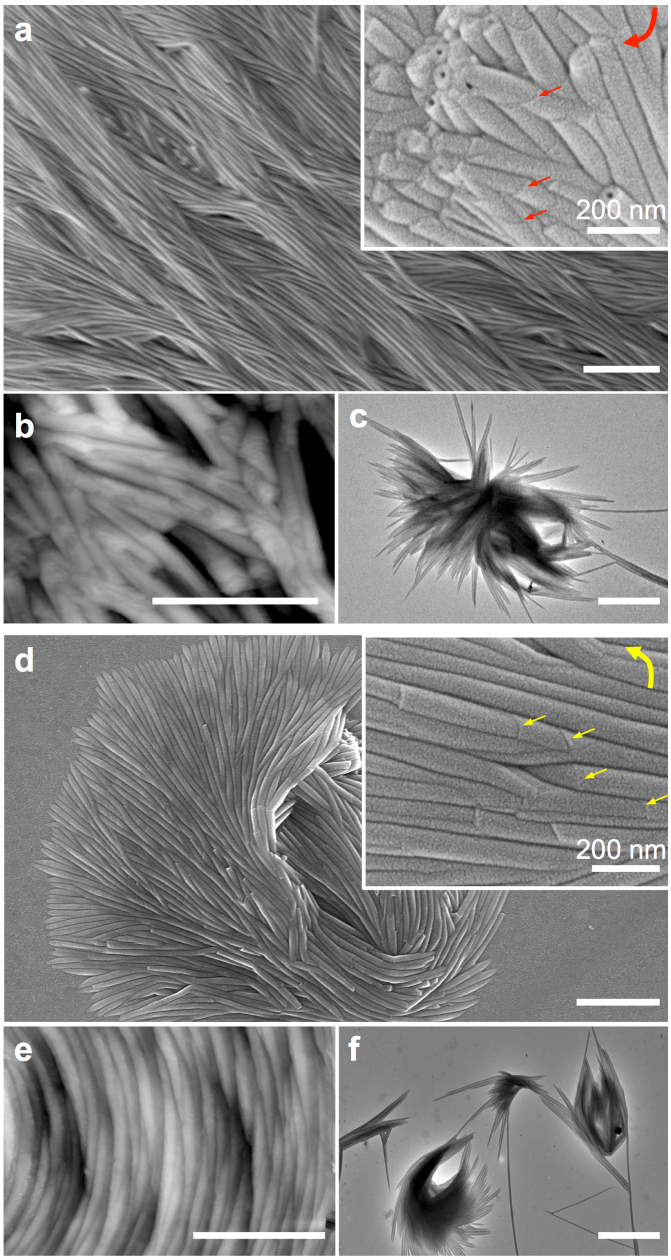

Fig. 4. (a) SEM image of the HLNCs of *p*-(*R*)-**4**; the inset shows a high resolution SEM that shows the left-handed heliconical wrapping of the layers (red arrows). (b) AFM image showing the solid nature and some peeled regions that revealed the layer thickness (for a height profile scan see ESI, Fig. S20). (c) TEM image of the HLNCs obtained from a slow cooled sample. (d) SEM image of the HLNCs of *p*-(*S*)-**4** (slow cooled sample), the inset shows a high resolution SEM that shows right-handed heliconical wrapping of the layers (yellow arrows). (e) AFM image, and (f) TEM image. Unless otherwise indicated, the scale bar in these images equals 1 µm. Several additional SEM, AFM and TEM images are collected in the ESI.

multi-walled nanocylinders that allowed for the measurement of the layer thickness (~ 4 nm), which is on the order of one molecular length in analogy to the XRD data (Figs. 4b and S21 – S23 in the ESI).

Bent-core LC molecules with acute bent angle (based on 1,7-substituted naphthalene central aromatic ring system), have been shown to form a closely related nanotube-like morphology. However, the formation of these tubes was only observed when the bent-core LC contained an admixed ~ 10 to 30 wt.% of a nematic or smectic LC. The neat bent-core compounds formed hexagonal columnar (Col_h) and highly porous sponge-like B4 phase morphologies.[22] The nanotubes formed by these mixtures featured ~ 7 layers with an overall diameter of 70-80 nm and an inner hole of ~ 20 nm. Other related superstructures were described, as stated earlier, by Hsu *et al.* in the form of helical twisted ribbons and tubular morphologies composed thereof, crystalline in nature, which formed when a related bent-core LC molecules with one chiral side chain ((*R*)- and (*S*)-enantiomer) were initially dissolved in isopropyl alcohol and allowed to stand for extended periods of time.[18] These superstructures, however, formed in the gel state, as reported by Górecka and co-workers for bent-core LCs with a flexible central hydrocarbon spacer,[19] and not in the bulk liquid crystal phase as reported here. In analogy to these gelation experiments, we also examined the morphology of the superstructures formed by *p*-(*R*)-**4** and *p*-(*S*)-**4** after dissolving them (and allowing them to stand) in *n*-hexane. SEM images (Fig. S24, Section 9, ESI) reveal the striking similarity of these formed superstructures to those observed in the bulk materials after thermal treatment. The only difference is the shorter length of the HLNCs (now only 1 to 2 μm).

To further study the HLNCs formed in the bulk LC phase we performed TEM analysis of *p*-(*R*)-**4** and *p*-(*S*)-**4** after slow cooling from the isotropic liquid phase. These TEM images illustrate that the nanocylinders are not usually hollow, but solid, and that they self-assemble into rather unique shapes (Fig. 4c). In a few areas of several SEM images it appears that the inner core of these coaxial cylinders grows faster, in others slower, leading to both pointed solid and what looks like hollow coaxial cylinders, respectively. Similar images were also obtained for *p*-(*S*)-**4** (Figs. 4d-f). If we take branching points as a point of reference for the direction of growth, the images also show that *p*-(*R*)-**4** forms left-handed heliconical layers and *p*-(*S*)-**4** right-handed heliconical layers (insets in Figs. 4a and 4d). Also striking, larger sample thicknesses (by simply depositing more material) lead to nest-like texture formed by nanocylinders (Fig. 4d). This appears to be a direct result of nanocylinders either merging or splitting, which then leads to curvature. When the material is confined between two substrates during the heating/cooling protocol, the nanocylinders typically form tangentially coiled up structures with no space between them, which is shown by AFM of such samples after one of the two substrates is removed (Fig. 4e). TEM images of both materials confirm the nest-like structures being hollow in the center (see, for example, Fig. 4f), which infers the tendency of the nanocylinders to roll up in confinement or when deposited onto thicker films substrates.

SEM images of the rapidly cooled bulk samples of *p*-(*R*)-**4** and *p*-(*S*)-**4** after heating to the isotropic liquid phase clearly support the biphasic nature of the resulting room temperature phases. Areas of bunched HLNCs are mixed with smooth regions from the surrounding columnar LC phase (ESI, Figs. S19a and S19c).

Overall, compounds **4** with the chiral side-chain on the *para*-side of the bent-core show a remarkable hierarchical self-assembly that is distinctly different from the other derivatives of the series. Compound **1** forms a B4 phase consisting of a conglomerate of equal proportions of left- and right-handed modulated HNFs, the two homochiral compounds **2** homochiral dual-modulated HNFs, and compounds **3** either a columnar phase or a B4 phase made up of homochiral helical microfilaments solely depending on the cooling rate from the isotropic liquid phase. Simply moving the chiral side-chain from the *meta*- to the *para*-side of the molecule now results in coaxial layered nanocylinders (of about 10 layers and 4 nm – the length of one molecule – layer thickness) with a heliconical twist depending on the absolute configuration of the chiral center. Furthermore, the coaxial-layered nanocylinders split (chirality preserving, like HNFs), grow tens of microns in lengths, align parallel or form feathered structures, braid, and finally grow to form birds nest-like structures with a hollow core. Revisiting the layer structure itself, what is difficult to determine is the packing within the layers. The layer thickness determined by AFM suggests there is little to no tilt of the molecules within the layers. The coaxial layer structure is similar to that of the so-called B7 texture formed either on cooling from the isotropic liquid phase[23] or developing at the polar interface to air.[24] However, in the B7 phase the equilibrium diameter of the B7 filaments is in the micrometer range, here the diameter is around 80 nm. Molecules forming the B7 textures generally have one or multiple functional groups or atoms larger than H attached to the central or outer benzene rings of the bent-core that serve as sterically demanding groups within the structure. A model that accounts for the steric and entropic interactions showed that such sterically demanding groups lead to spontaneous layer bend in the B7 textures.[25]

The heliconical layering along the nanocylinders' long axis (Figs. 5a) is also somewhat analogous to the layer modulations found in B7 textures[26], although in B7 materials the periodicity of the modulation is in the 10 nm range, whereas here it is a few hundred nanometers. Compounds **1** and **2**, with either no or two chiral centers respectively, form HNFs and compounds **3**, with a chiral center in the *meta*-side, form HμFs with negative Gaussian curvature, but molecules **4** form HLNCs with cylindrical curvature. Hence, relocating methyl groups within these molecules affects the curvature of the layers leading to the observed distinct morphologies.

A graphical summary of the observed multi-level hierarchical self-assembly together with typical SEM images is given in Fig. 5. One could count six levels of self-assembly starting from the packing of the constituent bent-core molecules into layers all the way to the formation of hollow circular structures (as in Fig. 5f, and in some cases even more

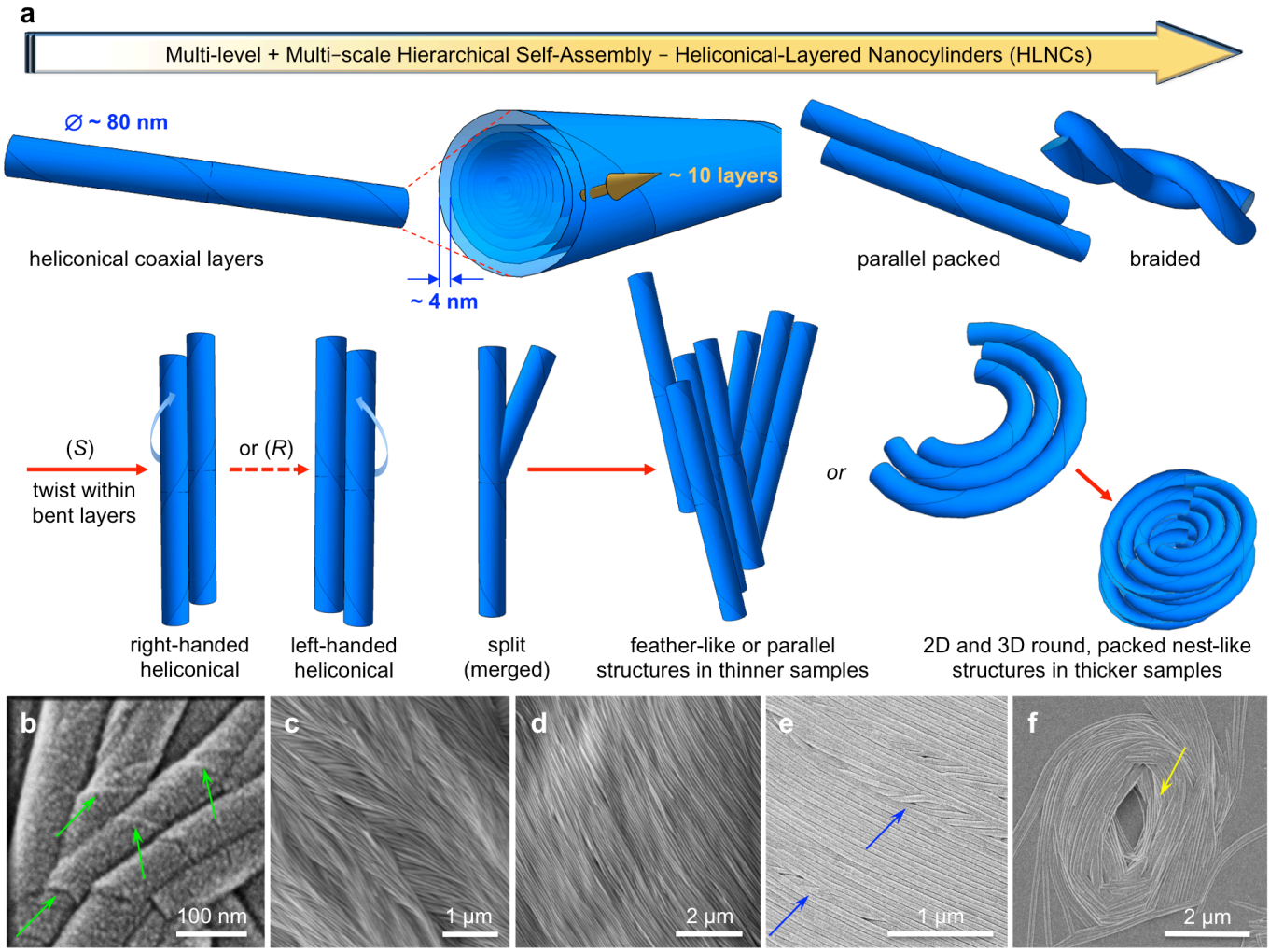

Fig. 5. (a) Models of packing of *p*-(*R*)-**4** and *p*-(*S*)-**4** in HLNCs and packing modes found for the HLNCs. (b – f) Representative SEM images for the heliconical layers forming the nanocylinders (green arrows in (b)) and the various packing modes (e.g., braided - blue arrows in (e) and birds nest-like – yellow arrow in (f)) observed by SEM, AFM, and TEM.

defined geometric objects as in Figs. S19, S20, and S23 in the ESI) additionally characterized by blue structural color in reflection (ESI, Fig. S25). A comparison could be made to the hierarchical self-assembly in skeletal muscle fibers. Here, however, multiple molecular as well as cellular building blocks are needed to achieve this, including myosin, thin actin filaments, and the sarcoplasmic reticulum.[27]

Molecules *p*-(*R*)-**4** and *p*-(*S*)-**4** studied here are asymmetric and contain a sterically demanding chiral center in the side chain of the *para*-side. We propose that the sterically demanding structural elements in the side-chain of the *para*-side are responsible for the formation of the nanocylinders. Due to these chiral centers the direction or orientation of the (*R*)- or (*S*)-CH_3 group is rotating within and across the layers affecting the equilibrium layer bend. At the center of the cylinders should be a defect where the material is melted. Moving outside, where the first curved layers form with the largest curvature, the CH_3 group is likely in the plane of the cross section. In subsequent layers the CH_3 group eventually turns normal to the cross section at the quarter pitch, *p*,

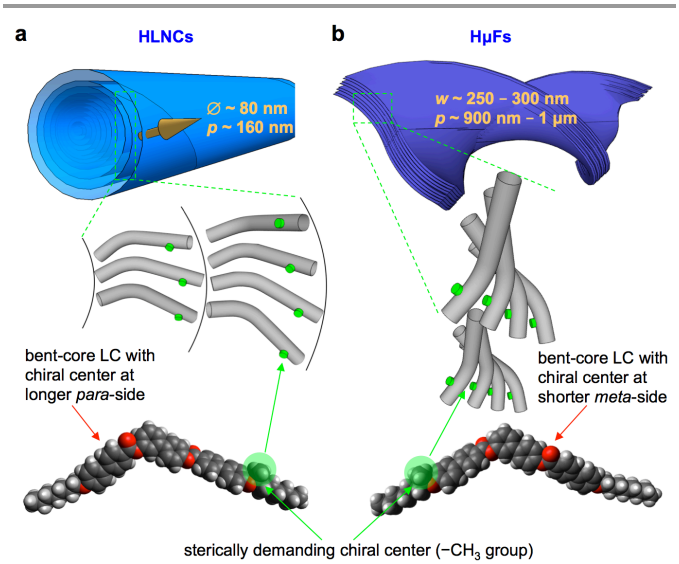

Fig. 6. Purely geometric (steric) models to visualize the formation of: (a) HLNCs by *p*-(*R*)-**4** and *p*-(*S*)-**4** and (b) HµFs by *m*-(*R*)-**3** and *m*-(*S*)-**3**.

distance. Once more layers are added, the CH_3 group would turn inside the cross section again, which would be compatible only with increasing curvature, so the cylinder should terminate at a radius $r = p/4$. The observed radius of ~ 40 nm of the cylinders indicates a helical pitch of about p ~ 160 nm (Fig. 6a). Contrary, *m*-(*R*)-**3** and *m*-(*S*)-**3** reported earlier[12] with the sterically demanding chiral centers in the shorter *meta*-side appear to release the steric strain by twisting rather than bending (Fig. 6b). To support these more simplistic geometric models, we performed detailed computational studies of the (*R*)-enantiomers (*m*-(*R*)-**3** and *p*-(*R*)-**4**), representatively, in an attempt to identify any features that may be important in contributing to the different superstructures (morphologies) displayed by the chiral bent-core mesogens **3** and **4** (for details see Section 11, Figs. S26 and S27 and Table S2, ESI).

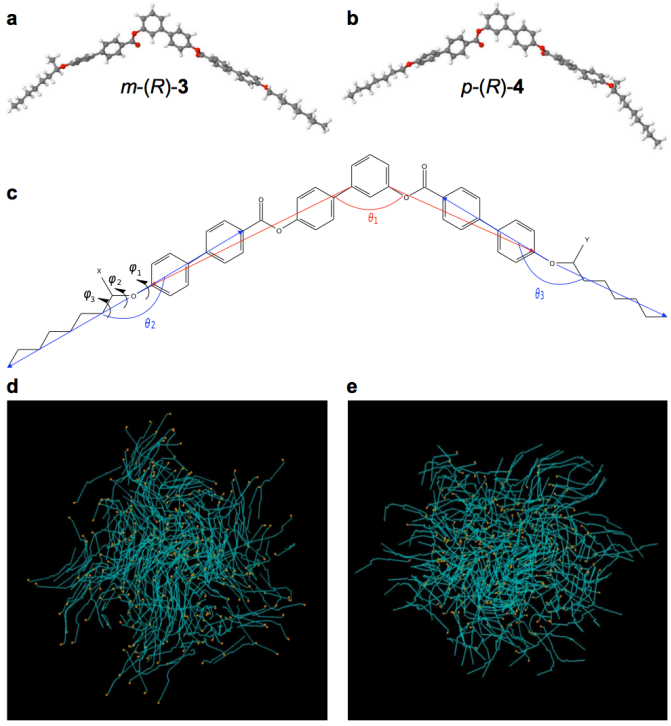

Fig. 7. Lowest energy geometries obtained at the B3LYP/6-311(d,p) level of theory for (a) *m*-(*R*)-**3** and (b) *p*-(*R*)-**4**. (c) Chemical structure and definitions of angles and dihedrals analyzed. [*p*-(*R*)-**4**, X = CH_3, Y = H, *m*-(*R*)-**3**, X= H, Y = CH_3]. Simplified representations of snapshots from the molecular dynamics simulations (N = 256 molecules) of: (d) *m*-(*R*)-**3** at T = 350 K and (e) *p*-(*R*)-**4** at T = 380 K. Chiral centers are highlighted in orange. For larger images see ESI, Fig. S28.

Because such minor chemical modifications lead to such significant geometrical changes in the final superstructures, we first examined the geometry of each mesogen, as molecular shape is an important parameter in determining LC phase structure as well as stability.[28, 29] The lowest energy geometries obtained from DFT methods are shown in Fig. 7a and 7b. Initial observations suggest that the chiral center induces a change from a linear projection of the alkyl chain relative to the aromatic core, to a more bent projection of the alkyl chain, whether it is located on the *meta*- or the *para*-side. The effect appears more pronounced when the chiral center migrates from the *meta*- to the *para*-side (the longer arm) resulting in the overall molecular geometry of *p*-(*R*)-**4** appearing more curved compared with that of *m*-(*R*)-**3**.

The actual shape of a molecule is difficult to define as a range of conformations will determine this, and therefore a useful procedure is to calculate various angle and dihedral distributions. The region where core and aliphatic hydrocarbon chain encounter one another plays an important role in structure-property relationships of LCs.[30] Any differences in core-chain geometries between *m*-(*R*)-**3** and *p*-(*R*)-**4** are therefore likely to lead to distinct conformations which may affect the packing density of the mesogens, resulting in specific phase structures.[31]

Single molecule stochastic dynamics (SD) atomistic simulations allow a range of molecular conformations to be sampled, rather than a single optimized conformation. Firstly, the angle distribution for the bent aromatic core (defined as angle θ_1 in Fig. 7c) was calculated and found to be almost identical for both molecules (Fig. S26). A narrow major peak occurs in the angle distribution function at approximately 120°, a value typical for bent-core mesogens containing a central phenyl ring.[32] To examine the effect of the chiral center on either the *meta*- or *para*-chain of the mesogens, core-chain angle distributions were also calculated. The core-chain angle distribution for θ_2 of *m*-(*R*)-**3** displays a broader distribution of peak values occurring between 130° to 160°. An even broader distribution of angles and a noticeable shift to lower values is apparent for the core-chain angle, θ_3, with peak values for the angle distribution function occurring between 100° to 140°. A similar effect is also observed for *p*-(*R*)-**4**, but in this instance the effect occurs for the longer arm, where the presence of the chiral center promotes a significant shift to lower bend angles between the core and chain compared with that for the shorter arm. This suggests that the effect of the chiral center is to induce a conformational change to a more bent shape at the core-chain junction compared to that for the longer arm lacking a chiral center in *m*-(*R*)-**3**.

Additional information on the core-chain geometry can be obtained from examining various dihedral distribution functions. Fig. S27 shows the dihedral distributions for φ_1, φ_2 and φ_3 for the *para*-side (longer chain) of *m*-(*R*)-**3** and *p*-(*R*)-**4**. The presence of the chiral center results in some distinctive differences in these distributions. It can be seen that the profiles for *m*-(*R*)-**3** are all symmetric (Fig. S27a). Major peaks occur at 180° for dihedrals φ_1 and φ_2, consistent with predominantly *trans*-conformations and hence a geometry corresponding to the O-CH_2 bond lying in the same plane as that of the aromatic ring, as has been previously reported for alkyloxy-ring junctions.[33] Dihedral φ_3, located further away from the core, appears more flexible, with peaks of a similar magnitude at φ_3 = 64°, 180° and 294°. In sharp contrast, the distributions for the analogous dihedral angles for *p*-(*R*)-**4** (Fig. S27b) containing the chiral center on the *para*-side of the mesogen, are strongly distorted, with major peaks predominantly moving away from 180° (i.e. from the *trans*-conformation). For example, the major peaks for both φ_1 and φ_2 are offset by ≈ 12° and 15°, respectively, relative to 180°, and the distribution for φ_3 shows a dominant peak at 294°.

This suggests that the introduction of chiral center on the *para*-side chain changes the local topology of the connection of the alkoxy chain to the molecular core.

Although it is expected that the same dihedral distributions adjacent to the core of the meta side of *m*-(*R*)-**3** containing a chiral center will be similar, it is possible that the presence of the chiral center on the longer arm exerts a greater influence on the overall molecular shape and chirality of the molecule than when the chiral center is located on the *meta*-side. In particular, the non-symmetric structure of the aromatic core, which creates an extended core on the *para*-side, coupled with the preferred non-planar arrangement of the inter-ring dihedral of the biphenyl units[34] and ester linkage groups,[35] may lead to more opportunity for twisted conformations for this arm as suggested already in Fig. 6a.

The dihedral distribution functions suggest that placement of the chiral center on the *para*-side of the molecules appears to further increase the bent-twisted nature of this arm, which in turn may exacerbate the mismatch between the two halves of the bent-core molecules. In contrast, placing the chiral center on the *meta*-side as in *m*-(*R*)-**4** evens out the relative twists of the two halves, leading to less of a mismatch between the two arms in terms of overall chiral shape. It has been proposed that the mismatch between the two molecular arms of bent-core mesogens leads to dilation in one half-layer and compression in the other, and is a driving force in the development of HNFs[5] or specifically HμFs as reported for *m*-(*R*)-**3** and *m*-(*S*)-**3**.[12] The degree of mismatch between the two molecular arms appears to be enhanced for *p*-(*R*)-**4** compared with *m*-(*R*)-**3** and may be a factor in promoting the distinctly different morphologies observed for the two sets of materials.

Changes in conformational distributions between the two sets of compounds may also be expressed in terms of changes in average molecular dimensions (see ESI, Section 11 and Table S3). Finally, Figs. 7d and 7e show equilibrated snapshots of preliminary fully atomistic simulations of *m*-(*R*)-**3** and *p*-(*R*)-**4** at temperatures in their respective B4 phases. To see the organization of the systems more clearly, a single was plotted line through the central molecular bent-core unit, up to and including the chiral center. Visual inspection of the simulations indicates that both systems display an overall helical arrangement of the bent-core molecules. However, the helical arrangement of *m*-(*R*)-**3** appears to be more consistent with a corkscrew-type (Fig. 7d). In contrast, *p*-(*R*)-**4** appears to show some degree of aggregation of the bent-cores into curved layers (Fig. 7e), which is less apparent in *m*-(*R*)-**3**, although the fact that the view is through a three-dimensional simulation box means that clearly discerning helical twisted layers can be difficult. It can be seen that a second noteworthy difference between the two systems is the presence of negative curvature in the *m*-(*R*)-**3** system (Fig. 7d) where distinctive scallop-like outer surfaces are clearly visible, as opposed to the more globular overall appearance of the *p*-(*R*)-**4** system, further supporting our earlier argument of either negative Gaussian and cylindrical curvature for compounds **3** and **4**, respectively. Notably, related heliconical (helical) or twisted ribbons with negative Gaussian or cylindrical curvature have been reported for surfactant bi- and multilayer motifs.[36, 37]

Conclusions

The experiments and computational data summarized here strongly suggest that there must be other cases of such rich morphological and structural variety, not just among bent-core but also for other complex LC systems. Imaging techniques including electron and atomic force microscopy will play an increasingly important role in exploring new and revisiting previously described materials. In conclusion, the morphology described here appears to be among the most complex self-assembled structures ever reported for LCs, and overall a fairly unique system with remarkably rich structural and shape polymorphism considering the very small number of closely related compounds considering their chemical structure. The formation of distinct self-assembled superstructures appears to depend on subtle changes in the overall molecular shape caused by small changes in local molecular conformations. This also emphasizes that the final hierarchical self-assembled superstructures are energetically very close, which should provide opportunities for the discovery of other not yet reported morphologies, and perhaps combinations thereof, as we map out the structural space of these and related bent-core LC materials. Finally, we would like to highlight that the new type of polymorphism solely depending on the cooling rate, formerly observed for the *meta*-**3** molecules between columnar and B4 phase, resides exclusively with the columnar phases for the *para*-**4** molecules. Ongoing and future work will focus on more elaborate MD simulations that will directly feed into studies involving elasticity theory and shape selection as well as layer bend and twist resulting in the various types and degree of curvature observed for HNFs, HμFs and HLNCs.

Conflicts of interest

There are no conflicts to declare.

Author contributions

S.S., L.L., S.L.W., and J.P.V. performed synthesis and analytical characterization, S.S. the POM and SEM studies, A.N. the TEM and S.S. as well as A.N. the CD studies. M.S. performed the XRD, M.E.P. and E.H. the synchrotron SAXS experiments. M.S. and C.Z. performed the analysis of the XRD data. M.S. did the AFM imaging. N.J.B. and M.R.W. performed DFT calculations and atomistic simulations. A.I.J. and T.H. jointly directed the study, and T.H. with contributions from all co-authors wrote the manuscript.

Acknowledgements

The work was financially supported by the U.S. National Science Foundation (NSF, DMR-1506018 and CHE-1659571), the Ohio Third

Frontier program for Ohio Research Scholars "Research Cluster on Surfaces in Advanced Materials" (T.H.), which also supports the Liquid Crystal Characterization facility at the Liquid Crystal Institute (KSU) where some of the current SEM data were acquired. We also acknowledge access to and the help by Dr. D. Wang for SEM at the Swagelok Center for Surface Analysis of Materials at Case Western Reserve University, and thank Northeast Ohio Medical University for access to TEM. We are also grateful for access to the beamline 7.3.3 at the Advanced Light Source (Lawrence Berkeley National Laboratory), which are supported by the Director (Office of Science, Office of Basic Energy Sciences) of the U.S. Department of Energy under Contract No. DE-AC02-05CH11231. N.J.B. and M.R.W. would like to thank Durham University for computer time on its Hamilton HPC facility. M.S. acknowledges the support of the National Science Center (Poland); grant 2016/22/A/ ST5/00319. We thank the University of Warsaw for access to the XRD and AFM facilities.

Notes and references

1. D. R. Link, G. Natale, R. Shao, J. E. Maclennan, N. A. Clark, E. Korblova and D. M. Walba, *Science*, 1997, **278**, 1924-1927.
2. L. E. Hough, M. Spannuth, M. Nakata, D. A. Coleman, C. D. Jones, G. Dantlgraber, C. Tschierske, J. Watanabe, E. Korblova, D. M. Walba, J. E. Maclennan, M. A. Glaser and N. A. Clark, *Science*, 2009, **325**, 452-456.
3. V. Borshch, Y. K. Kim, J. Xiang, M. Gao, A. Jákli, V. P. Panov, J. K. Vij, C. T. Imrie, M. G. Tamba, G. H. Mehl and O. D. Lavrentovich, *Nat. Commun.*, 2013, **4**, 2635.
4. C. Dressel, T. Reppe, M. Prehm, M. Brautzsch and C. Tschierske, *Nat. Chem.*, 2014, **6**, 971-977.
5. L. E. Hough, H. T. Jung, D. Kruerke, M. S. Heberling, M. Nakata, C. D. Jones, D. Chen, D. R. Link, J. Zasadzinski, G. Heppke, J. P. Rabe, W. Stocker, E. Korblova, D. M. Walba, M. A. Glaser and N. A. Clark, *Science*, 2009, **325**, 456-460.
6. C. Zhang, N. Diorio, O. D. Lavrentovich and A. Jakli, *Nat. Commun.*, 2014, **5**, 3302.
7. G. Pelzl, S. Diele and W. Weissflog, *Adv Mater*, 1999, **11**, 707-724.
8. E. Tsai, J. M. Richardson, E. Korblova, M. Nakata, D. Chen, Y. Q. Shen, R. F. Shao, N. A. Clark and D. M. Walba, *Angew. Chem. Int. Edit.*, 2013, **52**, 5254-5257.
9. D. Chen, M. R. Tuchband, B. Horanyi, E. Korblova, D. M. Walba, M. A. Glaser, J. E. Maclennan and N. A. Clark, *Nat. Commun.*, 2015, **6**, 7763.
10. R. A. Callahan, D. C. Coffey, D. Chen, N. A. Clark, G. Rumbles and D. M. Walba, *ACS Appl. Mater. Interf.*, 2014, **6**, 4823-4830.
11. L. Li, M. Salamończyk, A. Jákli and T. Hegmann, *Small*, 2016, **12**, 3944-3955.
12. L. Li, M. Salamończyk, S. Shadpour, C. H. Zhu, A. Jákli and T. Hegmann, *Nat. Commun.*, 2018, **9**, 714.
13. N. Miyaura and A. Suzuki, *Chem. Rev.*, 1995, **95**, 2457-2483.
14. A. A. Thomas and S. E. Denmark, *Science*, 2016, **352**, 329-332.
15. R. A. Reddy and C. Tschierske, *J. Mater. Chem.*, 2006, **16**, 907-961.
16. H. Niwano, M. Nakata, J. Thisayukta, D. R. Link, H. Takezoe and J. Watanabe, *J. Phys. Chem. B*, 2004, **108**, 14889-14896.
17. S. C. Lin, T. F. Lin, R. M. Ho, C. Y. Chang and C. S. Hsu, *Adv. Funct. Mater.*, 2008, **18**, 3386-3394.
18. S. C. Lin, R. M. Ho, C. Y. Chang and C. S. Hsu, *Chem.-Eur. J.*, 2012, **18**, 9091-9098.
19. A. Zep, M. Salamończyk, N. Vaupotic, D. Pociecha and E. Górecka, *Chem. Commun.*, 2013, **49**, 3119-3121.
20. C. L. Folcia, I. Alonso, J. Ortega, J. Etxebarria, I. Pintre and M. B. Ros, *Chem. Mater.*, 2006, **18**, 4617-4626.
21. D. M. Walba, L. Eshdat, E. Korblova and R. K. Shoemaker, *Cryst. Growth Des.*, 2005, **5**, 2091-2099.
22. E. Górecka, N. Vaupotič, A. Zep and D. Pociecha, *Angew. Chem. Int. Edit.*, 2016, **55**, 12238-12242.
23. G. Pelzl, S. Diele, A. Jákli, C. Lischka, I. Wirth and W. Weissflog, *Liq. Cryst.*, 1999, **26**, 135-139.
24. A. Jákli, D. Kruerke and G. G. Nair, *Phys. Rev. E*, 2003, **67**, 051702.
25. C. Bailey and A. Jákli, *Phys. Rev. Lett.*, 2007, **99**, 207801.
26. D. A. Coleman, J. Fernsler, N. Chattham, M. Nakata, Y. Takanishi, E. Korblova, D. R. Link, R. F. Shao, W. G. Jang, J. E. Maclennan, O. Mondainn-Monval, C. Boyer, W. Weissflog, G. Pelzl, L. C. Chien, J. Zasadzinski, J. Watanabe, D. M. Walba, H. Takezoe and N. A. Clark, *Science*, 2003, **301**, 1204-1211.
27. R. Wroblewski and E. Jansson, *Cell. Tissue Res.*, 1975, **161**, 471-476.
28. A. Pizzirusso, M. Savini, L. Muccioli and C. Zannoni, *J. Mater. Chem.*, 2011, **21**, 125-133.
29. G. Tiberio, L. Muccioli, R. Berardi and C. Zannoni, *ChemPhysChem*, 2009, **10**, 125-136.
30. G. Cinacchi and G. Prampolini, *J. Phys. Chem. A*, 2003, **107**, 5228-5232.
31. C. Keith, A. Lehmann, U. Baumeister, M. Prehm and C. Tschierske, *Soft Matter*, 2010, **6**, 1704-1721.
32. J. S. Lintuvuori, G. Yu, M. Walker and M. R. Wilson, *Liq. Cryst.*, 2018, **45**, 1996-2009.
33. S. Kaur, J. Addis, C. Greco, A. Ferrarini, V. Görtz, J. W. Goodby and H. F. Gleeson, *Phys. Rev. E*, 2012, **86**, 041703.
34. A. Pizzirusso, M. E. Di Pietro, G. De Luca, G. Celebre, M. Longeri, L. Muccioli and C. Zannoni, *ChemPhysChem*, 2014, **15**, 1356-1367.
35. T. Tsuji, H. Takeuchi, T. Egawa and S. Konaka, *J. Am. Chem. Soc.*, 2001, **123**, 6381-6387.
36. J. M. Schnur, *Science*, 1993, **262**, 1669-1676.
37. R. Oda, I. Huc, M. Schmutz, S. J. Candau and F. C. MacKintosh, *Nature*, 1999, **399**, 566-569.

